ChemComm

COMMUNICATION

View Article Online
View Journal | View Issue



Cite this: *Chem. Commun.*, 2024, **60**, 9558

Received 15th June 2024,
Accepted 8th August 2024

DOI: 10.1039/d4cc02900c

rsc.li/chemcomm



# Defect-rich $W_{1-x}Mo_xS_2$ solutions for efficient $H_2$ evolution in acidic electrolytes†

Zongge Li, *[a] Zhicheng Liu,[b] Danni Wang,[b] Wenjun Kang,[a] Haibo Li [a] and Guoxin Zhang *[b]

**An optimal $W_{0.4}Mo_{0.6}S_2$ solid solution, equipped with rich intrinsic defects, exhibits excellent stability in both 0.5 M $H_2SO_4$ and 2.0 M NaCl, showing negligible activity degradation after continuous 50 hours of working, thereby showing outstanding practical prospects.**

Hydrogen energy is an ideal energy storage medium coupling carbon-negative green electricity. Producing hydrogen through the electrochemical hydrogen evolution reaction (HER) in water electrolysis technologies would bring innumerable ecological environmental and economic benefits.[1] The high investment and operating costs have greatly limited its large-scale development owing to severe dependence on state-of-the-art precious metal Pt-based electrocatalysts.[2] Therefore, development of non-noble metal catalysts that are utilizable in harsh conditions (acidic and saline waters) is currently receiving enormous attention is yet of significant challenge.[3–5]

Transition metal dichalcogenides (TMDs), especially molybdenum sulfide ($MoS_2$) are promising candidates due to the high similarity of hydrogen adsorption/conversion chemistry to Pt.[6,7] However, their semiconductor properties limit the electronic transmission during the electrochemical process.[8] In addition, that makes substantial active sites distributed at the edges.[9] Thus, the construction of array structures, alien element doping, and other methods have been adopted to achieve higher edge activity.[10,11] Recent studies also suggest that introducing S defects in the basal plane benefits the optimization of the electronic structure of $MoS_2$ to enhance the overall electrocatalytic activity.[12,13] Electrochemical reduction, $H_2$ annealing, and argon plasma exposure were the general approaches used to remove S from the basal planes of $MoS_2$ partially, but were usually complicated and high operation temperatures were needed.[14–18] Developing a facile but efficient method to produce rich sulfur defects throughout $MoS_2$ materials remains challenging.

Herein, we develop a simple method that can *in situ* induce rich S defects in $W_{1-x}Mo_xS_2$ solid solution based on formamide chemistry, in which Mo and W atoms were firstly confined by rich N ligands derived from formamide.[19] Adopting the vulcanization operation enables formamide-derived N-doped carbonaceous materials to decompose gradually, creating a reductive atmosphere to promote the formation of S vacancies/defects on $W_{1-x}Mo_xS_2$ materials. Raman spectra and X-ray photoelectron spectroscopy (XPS) results confirmed the presence of abundant S defects. Electrochemical measurements demonstrated the coexistence of W and Mo with an optimal ratio of 4 : 6 and rich *in situ* formed S defects can significantly improve the HER activity in both 0.5 M $H_2SO_4$ and 2.0 M NaCl. An overpotential of only 203 mV *vs.* RHE is needed to achieve a current density of 10 mA $cm^{-2}$ in an acid electrolyte, which is much smaller than that for pure phase $MoS_2$ (281 mV *vs.* RHE) and $WS_2$ (277 mV *vs.* RHE). The $W_{0.4}Mo_{0.6}S_2$ sample also showed excellent activity stability for over 50 hours.

$W_{1-x}Mo_xS_2$ materials were prepared through a modified procedure involving (1) the anchoring of W/Mo species on formamide-derived N-doped carbonaceous materials and (2) annealing at high temperature in the presence of S vapor, as has been graphically depicted in Fig. S1 (ESI†). A range of molar ratios of W to Mo were adjusted to investigate its effect on HER activity. Firstly, the texture of the MoW-NC precursor was examined using scanning electron microscopy (SEM) (Fig. S2a, ESI†) and transmission electron microscopy (TEM) (Fig. S2b, ESI†), revealing the typical fine particle-stacking morphology of the MoW-NC-180 precursor. High-angle annular dark-field scanning transmission electron microscopy (HAADF-STEM) images (Fig. S2c, ESI†) suggest the even distribution of the W, Mo, C and N elements in the precursor. By utilizing XRD

[a] *Shandong Provincial Key Laboratory of Chemical Energy Storage and Novel Cell Technology, School of Chemistry and Chemical Engineering, Liaocheng University, Liaocheng 252059, China. E-mail: lizongge@lcu.edu.cn*

[b] *College of Energy Storage Technology, Shandong University of Science and Technology, Qingdao, Shandong 266590, China. E-mail: zhanggx@sdust.edu.cn*

† Electronic supplementary information (ESI) available: Experimental section, TEM images, XRD, and Raman spectra of WMo-NC precursors, SEM images, XRD curves, BET analysis, XPS element survey, C 1s spectra of $W_{1-x}Mo_xS_2$, supplementary electrochemical data of $WS_2$, $W_{0.4}Mo_{0.6}S_2$ and $MoS_2$ including Tafel plots, ECSA measurements, EIS spectra, and XPS analysis of $W_{0.4}Mo_{0.6}S_2$ before and after long-term stability tests. See DOI: https://doi.org/10.1039/d4cc02900c

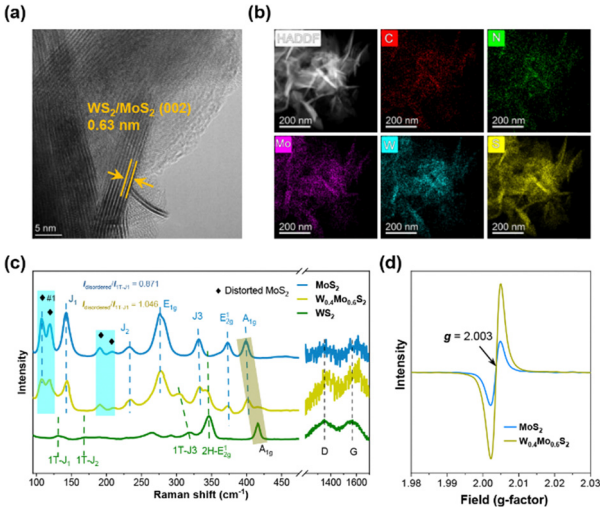


Fig. 1 (a) TEM image and (b) HRTEM-HAADF image and element mapping images of $W_{0.4}Mo_{0.6}S_2$. (c) Raman and (d) EPR spectra of $WS_2$, $W_{0.4}Mo_{0.6}S_2$, and $MoS_2$.

and Raman techniques (Fig. S3, ESI†), the MoW-NC precursor was shown to be a mixed configuration of $Mo_2C$ and graphitic carbon materials.

All the $W_{1-x}Mo_xS_2$ samples exhibit similar XRD patterns (Fig. S4, ESI†), suggesting the same crystal structure of 2H phase $MoS_2$ or $WS_2$. The diffraction peaks at 14.3°, 33.4°, 40.1°, and 58.5° are well in agreement with the (002), (101), (103), and (110) planes of hexagonal 2H-$MoS_2$ (JCPDS 37-1492). The pure phases of $MoS_2$ and $WS_2$ (JCPDS 08-0237) were also prepared for comparison. SEM images (Fig. S5, ESI†) reveal the typical flower-like infrastructure upon the introduction of W. For the $W_{0.4}Mo_{0.6}S_2$ sample, diverse lattice fringes with an interplanar distance of 0.63 nm corresponding to the (002) plane of $MoS_2$ can be observed in higher resolution TEM (HRTEM) images (Fig. 1a), which are larger than that of natural $MoS_2$ (0.62 nm),[14] and which may be due to the presence of defects enlarging the interlayer space. The main elements of Mo, W, S, C, and N are evenly distributed, as displayed in Fig. 1b; the presence of C and N signals may arise from the residual N-doped carbon from the formamide-derived precursor.[20,21] The $N_2$ adsorption–desorption isotherms suggest that the $W_{0.4}Mo_{0.6}S_2$ possesses a larger surface area of 74.91 $m^2\ g^{-1}$ over $MoS_2$ (66.49 $m^2\ g^{-1}$) and $WS_2$ (44.48 $m^2\ g^{-1}$) (Fig. S6, ESI†).

Fig. 1c shows the Raman spectra of $MoS_2$, $WS_2$, and $W_{0.4}Mo_{0.6}S_2$. $W_{0.4}Mo_{0.6}S_2$ exhibits a similar pattern to that of pure phase $MoS_2$, confirming that the crystal structure of this solid solution bears more resemblance to that of $MoS_2$. The bands positioned at 276 and 372 $cm^{-1}$ can be assigned to the $E_{1g}$ vibration mode and the in-plane $E^1_{2g}$ vibration mode of 2H phase $MoS_2$.[20] The peaks located at 142, 233, and 331 $cm^{-1}$ correspond to the $J_1$, $J_2$, and $J_3$ peaks of 1T phase $MoS_2$, which should originate from the defect-induced phase transformation.[20] The peaks at 373 and 398 $cm^{-1}$ correspond to the $E^1_{2g}$ and $A_{1g}$ modes of $MoS_2$; when W is introduced into the lattice of $MoS_2$, both the $A_{1g}$ and $E^1_{2g}$ modes become broadened and show intensity attenuation, suggesting the different vibrations of the S atom due to the replacement of the W atom. Meanwhile, compared with the pure $MoS_2$, the $J_3$, $A_{1g}$, and $E^1_{2g}$ modes of $W_{0.4}Mo_{0.6}S_2$ shift to higher frequencies, demonstrating that crystal symmetry was broken to some extent. The minor bands located at 107, 119, 190, and 207 $cm^{-1}$ suggest that the lattice structure has been distorted owing to the largely altered structure during the *in situ* transformed process from W/Mo-NC to $W_{0.4}Mo_{0.6}S_2$ solution.[20,22] An indicator of the intensity ratio of the peak at 107 $cm^{-1}$ (disordered) to the 1T–J1 peak is made to compare the disordering extent, as marked in Fig. 1c, which shows that $W_{0.4}Mo_{0.6}S_2$ has an $I_{disorder}/I_{1T\text{-}J1}$ of 1.046, which is much larger than that of $MoS_2$ (0.871), implying that $W_{0.4}Mo_{0.6}S_2$ has a higher extent of defects. The broad peaks at 1359 and 1606 $cm^{-1}$ at the high frequency can be assigned to the disorder (D) and graphitization (G) bands of graphitic carbon. It is also noteworthy that $W_{0.4}Mo_{0.6}S_2$ also shows characteristic peaks of $WS_2$, the peaks at 305 and 344 $cm^{-1}$ that correspond to the emergence of $J_3$ and $E^1_{2g}$ modes of $WS_2$. In addition, the EPR spectra in Fig. 1d confirm that there appear strong signals at the *g* factor = 2.003 in the $W_{0.4}Mo_{0.6}S_2$ sample, confirming the existence of more sulfur vacancies in $W_{0.4}Mo_{0.6}S_2$ than in $MoS_2$.

The XPS survey (Fig. S7a, ESI†) identifies the presence of the W, Mo, S, C, and N elements in $W_{0.4}Mo_{0.6}S_2$. The elemental contents of $W_{0.4}Mo_{0.6}S_2$ measured by XPS suggest that the atomic ratio of W, Mo and S atoms was 0.35 : 1 : 2.28 (Table S1, ESI†). Fig. 2a shows that there is some energy overlapping between N 1s and Mo 3p, where the N species are mainly divided into pyridinic N, pyrrolic N, and graphitic N. The high-resolution Mo 3d spectrum (Fig. 2b) of $W_{0.4}Mo_{0.6}S_2$ displays two characteristic peaks around 229 and 232 eV, which can be attributed to the $3d_{3/2}$ and $3d_{5/2}$ branches for $Mo^{4+}$ species in the 2H phase. Compared to pure $MoS_2$, these are two peaks showing obvious negative shifts of ≈0.2 eV in $W_{0.4}Mo_{0.6}S_2$, proving that W doping in $MoS_2$ increases the surface electron density of Mo, which may benefit the release of H atoms on

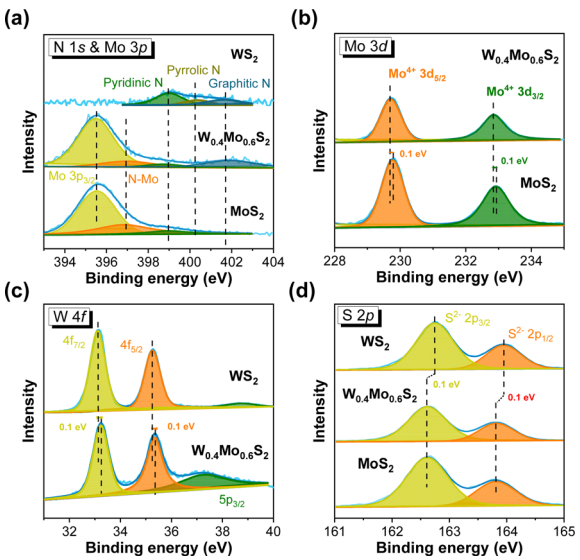


Fig. 2 XPS analysis of $WS_2$, $W_{0.4}Mo_{0.6}S_2$ and $MoS_2$: (a) N 1s and Mo 3p, (b) Mo 3d, (c) W 4f, and (d) S 2p spectra.

$MoS_2$, promoting the HER process.[23] For the XPS spectrum of W (Fig. 2c), three peaks located at 33.1, 35.2, and 37.4 eV correspond to the W $4f_{7/2}$, $4f_{5/2}$, and $5p_{3/2}$ branches, and there exists a slight negative shift of about 0.1 eV compared to that of pure $WS_2$, confirming the presence of $W^{4+}$ in $MoS_2$. As shown in Fig. 2d, two typical peaks at 162.5 and 163.7 eV are assigned to the S $2p_{3/2}$ and S $2p_{1/2}$ orbitals of the $S_2^-$ species in $W_{0.4}Mo_{0.6}S_2$, and the obvious negative shifts of 0.1 and 0.2 eV can be observed compared with that of pure phase $MoS_2$ and $WS_2$, indicating the reduced electron density which originates from the positively charged sulfur defect in $W_{0.4}Mo_{0.6}S_2$.[24,25] The above-compared evidence reveals a synergistic effect between W and Mo atoms that greatly affects the chemical states of S and therefore the performance of S sites.[23,26–28]

The HER performance was first measured in 0.5 M $H_2SO_4$. To reflect the real working conditions, all the linear sweep voltammetry (LSV) curves were presented without any iR-correction (Fig. 3a). The LSV curves demonstrate that all the samples show improved electrocatalytic activity compared to $MoS_2$ or $WS_2$; when the feeding molar ratio of W : Mo reaches 4 : 6 ($W_{0.4}Mo_{0.6}S_2$ as mentioned above), optimal HER electrocatalytic activity is achieved, which needs only 203 mV *vs.* RHE to reach a current density of 10 mA $cm^{-1}$, which is much smaller than that of $MoS_2$ (281 mV *vs.* RHE) and $WS_2$ (277 mV *vs.* RHE) (Fig. 3b). Tafel slopes are obtained from their LSV curves. $W_{0.4}Mo_{0.6}S_2$ displays the smallest Tafel slope value (74.95 mV $dec^{-1}$) among these $W_{1-x}Mo_xS_2$ samples (Fig. 3b and Fig. S8, ESI†), proving that it experiences a Volmer–Heyrovsky mechanism ($H^+(aq) + e^- \rightarrow H_{ads}$, $H^+(aq) + H_{ads} \rightarrow H_2(g)$).[29] The HER activity of $W_{0.4}Mo_{0.6}S_2$ is also measured in 1 M NaOH for comparison (Fig. S9, ESI†), and the $W_{0.4}Mo_{0.6}S_2$ shows a lower overpotential of 260.2 mV to obtain a current density of 10.0 mA $cm^{-2}$, which is almost 60 mV more sluggish than that in 0.5 M $H_2SO_4$.

The LSV curves were also normalized by the BET surface to eliminate the influence of surface area on catalytic performance evaluation (Fig. 3c); $W_{0.4}Mo_{0.6}S_2$ needs the smallest potential to reach the same current densities, implying the beneficial effect of W doping. Cyclic voltammetry (CV) measurements at pH = 7 phosphate buffer electrolyte (Fig. S10, ESI†) were conducted to estimate the number of active sites ($n$), and the LSV curves could be normalized by $n$ and expressed in the form of the turnover frequency (TOF) (Fig. 3d).[30–33] At the same potential of 250 mV *vs.* RHE, the TOF value for $W_{0.4}Mo_{0.6}S_2$ is 0.55 $s^{-1}$, which is 1.9 and 2.8 times that for the $WS_2$ (0.29 $s^{-1}$) and $MoS_2$ (0.19 $s^{-1}$), proving the high intrinsic per-site catalytic activity of $W_{0.4}Mo_{0.6}S_2$. Double-layer capacitance ($C_{dl}$) values were estimated from the CV curves from 20 to 120 mV $s^{-1}$ in a non-faradaic potential window of 0–0.2 V *vs.* RHE (Fig. S11, ESI†); the $W_{0.4}Mo_{0.6}S_2$ shows the highest $C_{dl}$ value of 17.0 mF $cm^{-2}$ compared to $WS_2$ and $MoS_2$, corresponding to the largest electrochemically active surface area (ECSA) (~117 $cm^2$), which is consistent with the BET surface area analysis, beneficial to the exposure of accessible active sites.[33] Fig. S12a (ESI†) displays the electrochemical impedance spectroscopy (EIS) curves, and the equivalent electrical circuit consisting of the solution resistance ($R_s$), constant phase angle element (CPE), and the charge transfer resistance ($R_{ct}$) was also provided.[34] The electrochemical impedance circuit fitting and the values of these parameters can be found in Fig. S12b–d and Table S2 (ESI†). The $W_{0.4}Mo_{0.6}S_2$ has the smallest $R_{ct}$ of 2.93 Ω, indicating the quickest electron transfer rate during electrocatalysis. The HER electrochemical performance of the $W_{0.4}Mo_{0.6}S_2$ is superior to or at least parallel to that of previously reported sulfides, as summarized in Fig. S13 (ESI†). Besides, the $W_{0.4}Mo_{0.6}S_2$ also shows very good durability, as shown in Fig. 3e, at both high and low current densities of 70 and 10 mA $cm^{-1}$ for more than 20 h.

Thereafter, $W_{0.4}Mo_{0.6}S_2$ and $RuO_2$ were assembled into a two-electrode water electrolyzer to test the overall water-splitting performance. The overall water electrocatalysis, as shown in Fig. 3f, can be driven at a very low voltage of 1.51 V in 0.5 M $H_2SO_4$. It needs only a low potential of 1.78 V to drive the current density to 10 mA $cm^{-2}$. Moreover, we also tested the overall water electrocatalysis electrochemical activity of the $W_{0.4}Mo_{0.6}S_2 \| RuO_2$ system in 2.0 M NaCl, which can be treated as a simulation of seawater splitting. As shown in Fig. 3f, about 2.0 V was needed to reach a current density of 10 mA $cm^{-2}$. Both in 0.5 M $H_2SO_4$ and in 2.0 M NaCl, the activities of $W_{0.4}Mo_{0.6}S_2$ can be maintained for at least 50 hours without obvious degradation (Fig. 3g). The XPS spectra of $W_{0.4}Mo_{0.6}S_2$ after the long-term stability test in 0.5 M $H_2SO_4$ are displayed in Fig. S14 (ESI†). As examined, very close curve patterns are shown compared to those of fresh $W_{0.4}Mo_{0.6}S_2$. After long-term operation in the harsh 0.5 M $H_2SO_4$ electrolyte, the $W_{0.4}Mo_{0.6}S_2$ still shows intact morphology and even distribution of Mo, W, and S (Fig. S14e and f, ESI†). Meanwhile, the elemental contents on the material surface display insignificant changes (Table S3, ESI†), suggesting a robust structure under harsh measuring conditions.

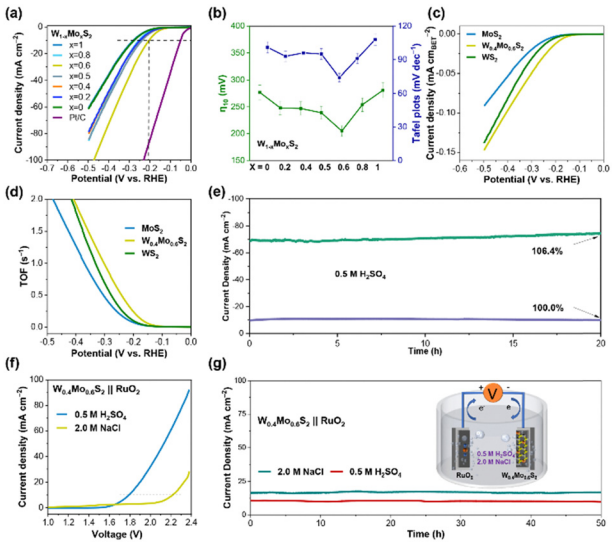


Fig. 3 Electrochemical measurements of $W_{1-x}Mo_xS_2$ and Pt/C in 0.5 M $H_2SO_4$: (a) polarization curves, (b) overpotentials at the current density of 10 mA $cm^{-2}$ ($\eta_{10}$) and Tafel slope of TOF curves, (c) polarization curves after normalized by BET surface area, (d) TOF curves, (e) long-term durability tests with a three-electrode setup. Water splitting measurement using $W_{0.4}Mo_{0.6}S_2 \| RuO_2$ in 0.5 M $H_2SO_4$ and 2.0 M NaCl: (f) LSV curves, (g) long-term stability test.

 

In summary, a facile and efficient method has been adopted to produce $W_{1-x}Mo_xS_2$ solid solutions possessing rich intrinsic S defects. The replacement of W on Mo atoms disturbs the crystal symmetry and allows a reductive atmosphere created by the combustion of the formamide-derived N-doped carbonaceous precursor to more profoundly impact the lattice structure, resulting in more abundant S defects for the enhancement of electrocatalytic HER activity. Indeed, the $W_{0.4}Mo_{0.6}S_2$ sample displays the best HER electrocatalytic activity among all the $W_{1-x}Mo_xS_2$ samples, requiring a very low overpotential of 203 mV *vs.* RHE to reach a current density of 10 mA $cm^{-1}$ in 0.5 M $H_2SO_4$, which is much smaller than that for $MoS_2$ and $WS_2$. Assembled with $RuO_2$ into a two-electrode water splitting system, a low cell voltage of 1.51 V was needed to drive the overall water electrolysis in 0.5 M $H_2SO_4$. Moreover, about 2.2 V was needed to reach a current density of 10 mA $cm^{-2}$ in 2.0 M NaCl. The $W_{0.4}Mo_{0.6}S_2$ also shows excellent activity retention and structural stability for continuously working in 0.5 M $H_2SO_4$ for over 50 hours, suggesting its practical application prospects in both acid water and seawater electrolysis.

Zongge Li: formal analysis, funding acquisition, methodology, writing – original draft. Zhicheng Liu: data curation, formal analysis, visualization. Danni Wang: investigation, software. Wenjun Kang: formal analysis, validation. Haibo Li: writing – review & editing. Guoxin Zhang: conceptualization, funding acquisition, project administration, writing – review & editing.

This work was financially supported by the National Natural Science Foundation of China (NSFC, No. 22071137, 22109090, and 22305109), the Natural Science Foundation of Shandong Province (No. ZR2023QB069), and the Research Projects of Liaocheng University (No. 318052271).

## Data availability

The data supporting this article have been included as part of the ESI.† The primary data that support the findings of this study are available from the corresponding author, Dr Z. Li or Dr G. Zhang, upon reasonable request.

## Conflicts of interest

There are no conflicts to declare.

## References

1 X. Yang, C. P. Nielsen, S. Song and M. B. McElroy, *Nat. Energy*, 2022, **7**, 955–965.
2 M. D. Bhatt and J. Y. Lee, *Energy Fuels*, 2020, **34**, 6634–6695.
3 X. Zou and Y. Zhang, *Chem. Soc. Rev.*, 2015, **44**, 5148–5180.
4 O. F. Aldosari, I. Hussain and Z. Malaibari, *J. Energy Chem.*, 2023, **80**, 658–688.
5 C. Wang, Q. Geng, L. Fan, J.-X. Li, L. Ma and C. Li, *Nano Res. Energy*, 2023, **2**, e9120070.
6 Y. Cao, *ACS Nano*, 2021, **15**, 11014–11039.
7 R. Li, J. Liang, T. Li, L. Yue, Q. Liu, Y. Luo, M. S. Hamdy, Y. Sun and X. Sun, *Chem. Commun.*, 2022, **58**, 2259–2278.
8 C. Sun, L. Wang, W. Zhao, L. Xie, J. Wang, J. Li, B. Li, S. Liu, Z. Zhuang and Q. Zhao, *Adv. Funct. Mater.*, 2022, **32**, 2206163.
9 A. Bruix, H. G. Füchtbauer, A. K. Tuxen, A. S. Walton, M. Andersen, S. Porsgaard, F. Besenbacher, B. Hammer and J. V. Lauritsen, *ACS Nano*, 2015, **9**, 9322–9330.
10 X. Wang, Y. Zhang, J. Wu, Z. Zhang, Q. Liao, Z. Kang and Y. Zhang, *Chem. Rev.*, 2021, **122**, 1273–1348.
11 Q. Xiong, X. Zhang, H. Wang, G. Liu, G. Wang, H. Zhang and H. Zhao, *Chem. Commun.*, 2018, **54**, 3859–3862.
12 Y. Ma, D. Leng, X. Zhang, J. Fu, C. Pi, Y. Zheng, B. Gao, X. Li, N. Li and P. K. Chu, *Small*, 2022, **18**, 2203173.
13 X. Guo, E. Song, W. Zhao, S. Xu, W. Zhao, Y. Lei, Y. Fang, J. Liu and F. Huang, *Nat. Commun.*, 2022, **13**, 5954.
14 J. Cai, Y. Xia, R. Gang, S. He and S. Komarneni, *Appl. Catal., B*, 2022, **314**, 121486.
15 Z. Luo, Y. Ouyang, H. Zhang, M. Xiao, J. Ge, Z. Jiang, J. Wang, D. Tang, X. Cao, C. Liu and W. Xing, *Nat. Commun.*, 2018, **9**, 2120.
16 C. Wang, H. Lu, K. Tang, Z. Mao, Q. Li, X. Wang and C. Yan, *Electrochim. Acta*, 2020, **336**, 135740.
17 M. Šarić, J. Rossmeisl and P. G. Moses, *J. Catal.*, 2018, **358**, 131–140.
18 A. Venkatalaxmi, B. S. Padmavathi and T. Amaranath, *Fluid Dyn. Res.*, 2004, **35**, 229.
19 G. Zhang, Y. Jia, C. Zhang, X. Xiong, K. Sun, R. Chen, W. Chen, Y. Kuang, L. Zheng and H. Tang, *Energy Environ. Sci.*, 2019, **12**, 1317–1325.
20 Z. Li, C. Li, J. Chen, X. Xing, Y. Wang, Y. Zhang, M. Yang and G. Zhang, *J. Energy Chem.*, 2022, **70**, 18–26.
21 Z. Li, C. Wang, A. Kumar, H. Jia, Y. Jia, H. Li, L. Bai, G. Zhang and X. Sun, *Adv. Powder Mater.*, 2023, **2**, 100138.
22 K. Qi, X. Cui, L. Gu, S. Yu, X. Fan, M. Luo, S. Xu, N. Li, L. Zheng, Q. Zhang, J. Ma, Y. Gong, F. Lv, K. Wang, H. Huang, W. Zhang, S. Guo, W. Zheng and P. Liu, *Nat. Commun.*, 2019, **10**, 5231.
23 Q. Xu, Y. Zhang, Y. Zheng, Y. Liu, Z. Tian, Y. Shi, Z. Wang, J. Ma and W. Zheng, *J. Phys. Chem. C*, 2021, **125**, 11369–11379.
24 J. Yang, H. Kawai, C. P. Y. Wong and K. E. J. Goh, *J. Phys. Chem. C*, 2019, **123**, 2933–2939.
25 J. Yang, F. Bussolotti, H. Kawai and K. E. J. Goh, *Phys. Status Solidi RRL*, 2020, **14**, 2000248.
26 L. Fan, S. Lei, H. M. Kheimeh Sari, L. Zhong, A. Kakimov, J. Wang, J. Chen, D. Liu, L. Huang, J. Hu, L. Lin and X. Li, *Nano Energy*, 2020, **78**, 105235.
27 G. Sun, F. Li, T. Wu, L. Cong, L. Sun, G. Yang, H. Xie, A. Mauger, C. M. Julien and J. Liu, *Inorg. Chem.*, 2019, **58**, 2169–2176.
28 X. Ren, Q. Wei, F. Wu, Y. Wang and L. Zhao, *Chem. Commun.*, 2021, **57**, 2531–2534.
29 J. Tian, Q. Liu, A. M. Asiri and X. Sun, *J. Am. Chem. Soc.*, 2014, **136**, 7587–7590.
30 D. Merki, S. Fierro, H. Vrubel and X. Hu, *Chem. Sci.*, 2011, **2**, 1262–1267.
31 Z. Pu, Q. Liu, C. Tang, A. M. Asiri and X. Sun, *Nanoscale*, 2014, **6**, 11031–11034.
32 P. Jiang, Q. Liu and X. Sun, *Nanoscale*, 2014, **6**, 13440–13445.
33 M. Li, M. Wang, D. Liu, Y. Pan, S. Liu, K. Sun, Y. Chen, H. Zhu, W. Guo, Y. Li, Z. Cui, B. Liu, Y. Liu and C. Liu, *J. Mater. Chem. A*, 2022, **10**, 6007–6015.
34 D. S. Dmitriev, A. A. Lobinsky and V. I. Popkov, *Colloids Surf., A*, 2021, **626**, 127007.